Design of Double-LCC-Compensated Wireless PMSM System With Variable DC-Link Voltage Considering Efficiency Optimization and Dynamic Improvement

Shuo Chen, *Student Member, IEEE*, Wen Ding, *Member, IEEE*, Lujie Huo, *Student Member, IEEE*, and Xiang Wu, *Member, IEEE*

***Abstract*—This article proposes a novel control strategy considering the efficiency optimization and dynamic improvement for dual-side LCC compensated wireless permanent magnet synchronous motor (PMSM) system with variable dc-link voltage. First, the dc-link voltage is added as a control variable to reduce the losses of three-phase converter. According to the variable dc-link voltage, the designing guidance about parameters of dual-side LCC compensation networks is given. Moreover, an extended state observer based voltage calculation method, robust to the parameter mismatch, is designed to obtain the minimum dc-link voltage reference required by PMSM system. A finite-control-set model-free predictive control is proposed for regulating the dc-link voltage to quickly track the reference. Furthermore, an adaptive perturbation and observation method is presented to improve the system efficiency, and the cooperative control principle of wireless PMSM system is given. Finally, the capability of proposed strategy is verified by experimental results.**

***Index Terms*—Dynamic improvement, efficiency optimization, model predictive control, variable dc-link voltage, wireless permanent magnet synchronous motor (PMSM) system.**

I. Introduction

WIRELESS power transfer (WPT), as one of the most promising technologies, has been gradually applied to many daily necessities and industrial products, including consumer electronics [1], biomedical implants [2], electrical vehicles (EVs) [3], underwater equipment, and so on, benefiting from its advantages of convenience, safety, high robustness, and long product lifespan. Recently, the concept of wireless motor system that ingeniously combining the WPT technology with various motor drive systems has aroused widespread attention from many scholars [4]. Different from the conventional motor drive system, the power cable is replaced by the magnetic coupler and the electric power can be transferred without any physical contacts in the wireless motor system. Hence, the wireless motor system is suitable for the harsh environments where the power cables are prone to be damaged or difficult to connect. For the in-wheel motors in EVs, the power cables are exposed to harsh environments and damaged due to the long-term corrosion and strong impact. The wireless-in wheel motor proposed in [5] and [6] can completely avoid the issue of wire breakage to improve the robustness of motor system. In the fields of high-speed railways, Kim et al. [7] designed a 1-MW WPT system-based power supply system to replace the overhead lines and pantographs, thereby increasing the reliability and maintenance the cost. Moreover, the risk of cutting power and signal wires limits the moving sphere of robots or robotic arms, and robots or robotic arms [8] driven by wireless motor systems undoubtedly avoid the wear and tear of wires. In piping networks, the combination of mobile energy carrying EVs and in-pipe wireless motor drives [9] can replace the large-scale underground power grid, so that the risk of network paralysis is avoided and the system cost can be significantly reduced.

Over several years, there are different types of wireless motor systems being developed. Jiang et al. [10] proposed a S-S compensated wireless dc motor system that separately controlling the armature and field currents by the time-division multiplexing. In [11], the wireless dc motor system with the bidirectional motion capability is further developed. Fang et al. [12] presented a wireless stepping motor system with four groups of coupling coils. But the use of carbon brush can lead to the low lifespan of the wireless motor system. Jiang et al. [13] proposed a novel S-S compensated wireless switched reluctance motor (SRM) system, where the one-to-three coil structure and two switch-controlled capacitors are adopted to implement a tunable compensation network. In [14], the LCC-S compensation network is used to avoid the extra switch-controlled capacitors. In [15], a x-type converter is further adopted to replace the structure of one-to-three coil in the LCC-S compensated wireless SRM system.

Manuscript received 18 August 2023; revised 1 November 2023; accepted 21 December 2023. Date of publication 26 December 2023; date of current version 26 January 2024. This work was supported by the National Natural Science Foundation of China under Grant 52077164. Recommended for publication by Associate Editor R. Zane. *(Corresponding author: Wen Ding.)*

Shuo Chen, Wen Ding, and Lujie Huo are with the School of Electrical Engineering, Xi'an Jiaotong University, Xi'an 710049, China (e-mail: ts17130047a3@cumt.edu.cn; wending@mail.xjtu.edu.cn; 3122304053@stu.xjtu.edu.cn).

Xiang Wu is with the School of Electrical and Power Engineering, China University of Mining and Technology, Xuzhou 221008, China (e-mail: cumtwuxiang@cumt.edu.cn).

Color versions of one or more figures in this article are available at https://doi.org/10.1109/TPEL.2023.3347076.

Digital Object Identifier 10.1109/TPEL.2023.3347076

However, the wireless SRM system suffers from the large torque ripples and noises. Moreover, the wireless single-phase shaded-pole induction motor systems are developed in [9], [16], and [17] as the wireless motor systems in pipeline transportations and in-pipe robots. Jin et al. [18] designed a S-S compensated wireless doubly-fed induction motor system for wind energy conversion fields. However, the power density and efficiency of induction motors are still limited.

Compared to different motors mentioned previously, permanent magnet synchronous motors (PMSMs) have the irreplaceable advantages of high torque density, high power density, and high efficiency. Several literatures [19], [20], [21], [22] have conducted research on the wireless PMSM system. In [19], the S-S compensated wireless PMSM system is designed for the application of in-wheel motor, where an extra buck–boost converter is employed. Furthermore, the LCC–LCC compensated PMSM system with matrix converter is presented in [20], where the buck–boost converter and dc-link electrolytic capacitor can be removed with the cost of the increased switching devices and complexity. In [21], a S-S compensated wireless open-winding PMSM system is subtly designed based on the one-two coil structure to enhance the fault-tolerant ability. Huang et al. [22] designed a novel three-phase six-stator-winding wireless PMSM, which controls the PMSM directly by the primary-side controller and avoids the use of secondary-side controller. However, the increasing passive components can reduce the efficiency and increase the system size. In addition, the guidance and procedure of parameter tuning of wireless motor system are not discussed in the abovementioned literatures. The improper system parameters may result in that the motor cannot operate under the rated working condition, or the low system efficiency is obtained due to the excessive power redundancy.

Efficiency has always been one of the most important indicators to evaluate wireless motor systems, but the strategies about efficiency optimization of wireless motor systems are rarely reported. In [19], the primary-side buck–boost converter is added to achieve the impedance matching of wireless PMSM system. However, the buck–boost converter will increase the size and cost of system and lead to the extra losses. Different from conventional PMSM systems, the dc-link voltage of wireless motor system is adjustable, and it can be added as a new variable to avoid the flux weakening control and reduce the converter loss at light-load condition [23], [24]. Chen et al. [25] subtly designed a perturbation observation (P&O) method-based dc-link voltage adjustment strategy for wireless PMSM system to track the maximum efficiency point, which is simple and naturally model-free. However, the continuous perturbation may affect the system stability and reduce the system efficiency. The passive component tuning method achieves the efficiency optimization by changing the values of passive components (inductance or capacitance) in real-time. The impedance matching is generally achieved through formula calculation method to adjust the phase shift angle or duty cycle of converter. But formula calculation method is based on ignoring the converter loss, and it depends on the system parameters [26]. This makes the system difficult to track the actual maximum efficiency point.

Furthermore, unlike the load of resistor or battery, the frequently varying working conditions of motors can lead to the severe impact on the dc-link voltage [27]. Hence, the stable and flexible dc-link voltage with fast dynamic is essential for wireless PMSM systems. In [19], the hysteresis control is adopted in the secondary-side for the stable dc-link voltage, which does not require any information from the primary-side. However, the hysteresis control could cause fluctuations in the currents and powers of wireless PMSM system. The S/P compensation network is adopted to prevent the voltage drop for wireless motor system in [25]. Chen et al. [27] proposed a feedforward voltage boost control strategy to enhance the dc-link voltage stability of wireless PMSM system. However, the dc-link voltage control is implemented on the primary-side controller, where a real-time fast wireless communication is necessary for the closed loop. The common wireless communication devices, such as Bluetooth, ZigBee, and Wi-Fi, have the long communication delay of milliseconds [28], which may affect the stability of dc-link voltage. The active rectifier or dc–dc converter added in the secondary side. The dc–dc converter active or rectifier on the secondary side can achieve the dc-link voltage without fast communication. The feedforward control [30] of dc–dc converter on the secondary side is presented to enhance the dynamic response of WPT system. But the extra dc–dc converters and current sensors increase the cost and size of system. In [31], a finite-control-set model predictive control (FCS-MPC) is presented for dynamic improvement of voltage regulation. Nevertheless, the control performance of MPC method depends on system parameters and extra current sensors.

For a wireless PMSM system, the reasonable parameter tuning principle, overall unit efficiency optimization, and fast tracking and stability of dc-link voltage are worthy of in-depth research. Aiming at the abovementioned issues, a novel control strategy considering efficiency optimization and dynamic improvement is proposed for the double-LCC-compensated wireless PMSM system. Since the dc-link voltage is related to the converter losses and voltage-limit constraint trajectory, the dc-link voltage is adjusted dynamically to reduce the losses of three-phase converter and avoid the flux weakening control. The minimum dc-link voltage reference is obtained by adopting the proposed extended state observer-based voltage calculation method (ESO-VCM), which robust to the parameter mismatch. Moreover, the capacity of wireless PMSM system varies with the dc-link voltage, which increases the difficulty of designing system parameters. The parameter tuning principle of wireless PMSM system with variable dc-link voltage is analyzed and given. For the fast tracking of dc-link voltage to reference provided by ESO-VCM, the finite-control-set model-free predictive control (FCS-MFPC) is presented for the dc-link voltage closed-loop control, where the accurate system parameters, extra sensors, and wireless communication are unnecessary. An adaptive P&O method with negligible steady-state perturbation is proposed to further improve the system efficiency. The overall cooperative control principle of the abovementioned methods for wireless PMSM system with variable dc-link voltage is also introduced. Only a slow wireless communication is needed to maintain the

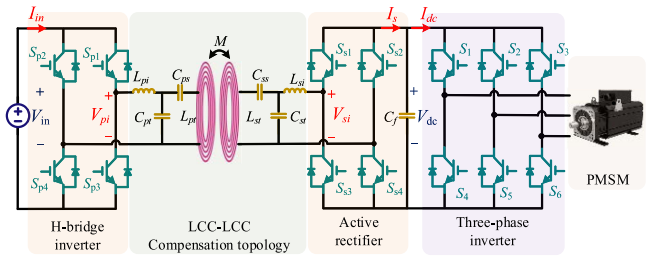

Fig. 1. Schematic diagram of double-LCC-compensated wireless PMSM system.

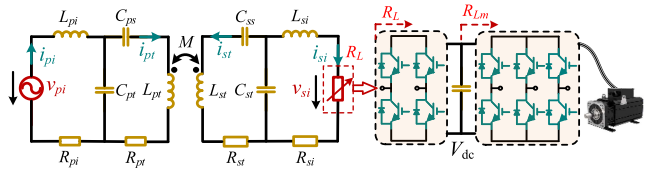

Fig. 2. Equivalent circuit of wireless PMSM system.

minimum power supply required by the system. Finally, the effectiveness of the proposed scheme is validated by experimental results.

II. Double-LCC-Compensated Wireless PMSM System

A. System Configuration

The schematic diagram of double-LCC-compensated wireless PMSM system is shown in Fig. 1. The wireless PMSM system consists of a H-bridge inverter, LCC–LCC compensation networks, an active rectifier, a three-phase inverter, and a PMSM. In the primary side, the dc voltage is converted to the ac voltage by the H-bridge inverter, so that the electric power can be transferred from the primary side to the secondary side through the double-LCC-compensated magnetic coupler. In the secondary side, the voltage is converted to the dc-link voltage for driving the motor system composed of a three-phase inverter and a PMSM. Ultimately, the power cable can be avoided, and the electric power can be converted to the mechanical power of motor system wirelessly. $V_{\rm in}$ and $V_{\rm dc}$ are the dc input voltage and the dc-link voltage, $I_{\rm in}$ and $I_{\rm dc}$ are the dc input current and the dc-link current, L_{pt} and L_{st} are the self-inductances of primary and secondary coils, and M denotes their mutual inductance. L_{pi}, L_{si}, C_{pt}, C_{ps}, C_{ss}, and C_{st} are the LCC–LCC compensation network' components. C_f denotes the filtering capacitor for the dc-link voltage.

The equivalent circuit of the wireless PMSM system is shown in Fig. 2. Due to the band-passing characteristic of LCC–LCC compensation network, fundamental harmonic approximation is generally used for ease of analysis. For the WPT system, the load composed of three-phase inverter and PMSM can be considered as a constant power load (CPL), which is equivalent to an adjustable resistive load R_{Lm}. The equivalent resistive load R_{Lm} can be represented as

$$R_{\rm Lm} = V_{\rm dc}^2 / P_{\rm dc} \tag{1}$$

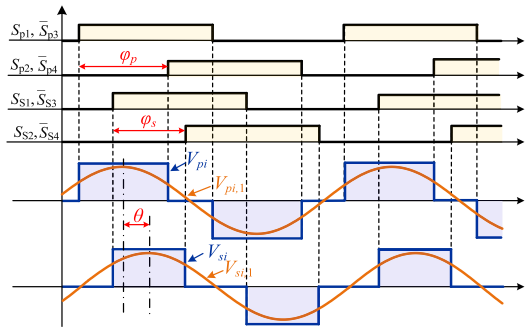

Fig. 3. Waveforms of H-bridge inverter and active rectifier under the PSC control.

where $P_{\rm dc}$ is the input power of the three-phase converter. Then, the equivalent resistance of CPL is described as

$$R_L = 8R_{\rm Lm}/\pi^2 = 8V_{\rm dc}^2/\pi^2 P_{\rm dc}. \tag{2}$$

It is obvious that the output power of the wireless motor system is determined by the dc-link voltage and the motor system's input power. Hence, for the wireless PMSM system, it is necessary to achieve the fast and robust regulation of the dc-link voltage, rotor speed, and electromagnetic torque.

B. Basic Control Scheme of Wireless PMSM System

In the wireless PMSM system, both H-bridge inverter, active rectifier and three-phase inverter require to be controlled jointly. The phase shift control (PSC) [26] is adopted to achieve the control of H-bridge inverter and active rectifier for the stable dc-link voltage regulation. Then, the dc-link voltage and space vector pulsewidth modulation (SVPWM) are combined to generate the driving signals for the three-phase inverter to drive the PMSM.

First, the main waveforms of H-bridge inverter and active rectifier under the PSC control are shown in Fig. 3. φ_p and φ_s are phase shift angles of V_{pi} and V_{si} that are the output voltage of H-bridge inverter and the input voltage of active rectifier, respectively. θ is the phase shift angle between $V_{pi,1}$ and $V_{si,1}$. $V_{pi,1}$, and $V_{si,1}$ are the fundamental components of V_{pi} and V_{si}, respectively, which are derived by the Fourier series expansion as

$$\begin{aligned}\dot{V}_{pi,1} &= \frac{2\sqrt{2}}{\pi} V_{\rm in} \sin\left(\frac{\varphi_p}{2}\right) \angle 0, \dot{V}_{si,1} \\ &= \frac{2\sqrt{2}}{\pi} V_{\rm out} \sin\left(\frac{\varphi_s}{2}\right) \angle -\theta.\end{aligned} \tag{3}$$

Assuming that the parameters of LCC–LCC compensation network are symmetrical and the system is completely resonant, the characteristics impedance of the system can be described as

$$\begin{cases} \omega L_{pi} = \omega L_{si} = \frac{1}{\omega C_{pt}} = \frac{1}{\omega C_{st}} \\ \frac{1}{\omega C_{ps}} = \frac{1}{\omega C_{ss}} = \omega L_{pt} - \frac{1}{\omega C_{pt}} = \omega L_{st} - \frac{1}{\omega C_{st}}. \end{cases} \tag{4}$$

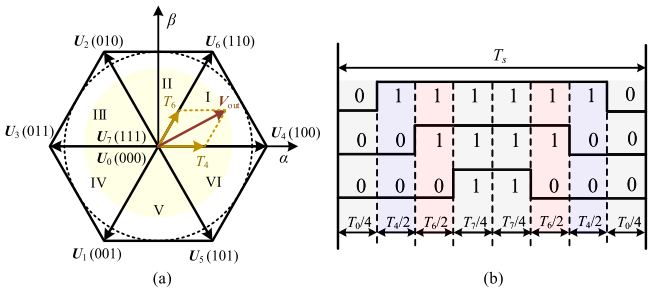

Fig. 4. Schematic diagram of mechanism of SVPWM. (a) Synthesized space voltage vector in sector I. (b) Switching sequence in sector I.

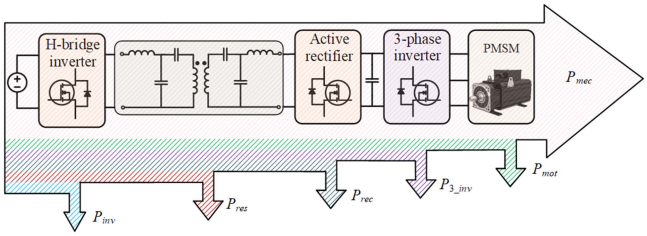

Fig. 5. Schematic diagram of power loss distribution of wireless PMSM system.

Ignoring the resistance loss and adopting the Kirchhoff's law, the transmitted active and reactive power can be calculated by

$$\begin{cases} P_{\text{out}} = \text{Re}\{\dot{V}_{si,1}\dot{I}^*_{si}\} = \frac{8k\sqrt{L_{pt}L_{st}}}{\pi^2\omega L_{pi}L_{si}} V_{\text{in}}V_{\text{dc}} \sin\left(\frac{\varphi_p}{2}\right) \\ \qquad \sin\left(\frac{\varphi_s}{2}\right)\sin(\theta) \\ Q_{\text{out}} = \text{Im}\{\dot{V}_{si1}\dot{I}^*_{si}\} = \frac{8k\sqrt{L_{pt}L_{st}}}{\pi^2\omega L_{pi}L_{si}} V_{\text{in}}V_{\text{dc}} \sin\left(\frac{\varphi_p}{2}\right) \\ \qquad \sin\left(\frac{\varphi_s}{2}\right)\cos(\theta) \end{cases} \tag{5}$$

where k denotes the coupling coefficient that satisfies $k = M/\sqrt{L_{pt}L_{st}}$. The phase shift angle θ is usually set to 90° for the zero reactive power and maximum efficiency transmission. Hence, the dc-link voltage V_{dc} is controlled by regulating the phase shift angles φ_p and φ_s.

After obtaining the stable dc-link voltage, the SVPWM scheme is applied to control the three-phase inverter for driving the PMSM. The mechanism of SVPWM in sector I is intuitively illustrated in Fig. 4 , where a voltage vector V_{out} is synthesized by two adjacent vectors and adopted as the required phase voltage for the PMSM. When the motor system is in the linear modulation region, the control period is reasonably divided into the action time of the nonzero vectors U_4 and U_6, and the zero vectors U_0 and U_7, as shown in Fig. 4(b).

C. Power Loss of Wireless PMSM System

Efficiency has always been one of the most important indicators to evaluate the wireless PMSM system. The schematic diagram of power loss distribution of wireless PMSM system is shown in Fig. 5. The total power loss P_{tot} of wireless PMSM system mainly composed of the resistance loss of resonant networks (P_{res}), and the conducting and switching losses of H-bridge inverter, active rectifier and three-phase inverter (P_{inv}, P_{rec}, and P_{3_inv}), and the copper and core losses of PMSM(P_{mot}), which is represented as

$$P_{tot} = P_{res} + P_{inv} + P_{rec} + P_{3\_inv} + P_{mot}. \tag{6}$$

The resistance loss of resonant networks is described as

$$P_{res} = I_{pi}^2 R_{pi} + I_{si}^2 R_{si} + I_{pt}^2 R_{pt} + I_{st}^2 R_{st}. \tag{7}$$

Moreover, the power losses of H-bridge inverter and active rectifier can be expressed as

$$\begin{cases} P_{inv} = P_{inv\_con} + P_{inv\_\text{sw}} \\ P_{rec} = P_{rec\_con} + P_{rec\_\text{sw}} \end{cases} \tag{8}$$

where P_{inv_con} and P_{rec_con} denote the conducting losses of H-bridge inverter and active rectifier, and P_{inv_sw} and P_{rec_sw} denote their switching losses, which can be calculated by

$$\begin{cases} P_{inv\_con} = 2I_{pi}^2 R_{DS} + 2\sqrt{2}V_f I_{pi}\left[1 - \sin\left(\varphi_p/2\right)\right]/\pi \\ P_{rec\_con} = 2I_{si}^2 R_{DS} + 2\sqrt{2}V_f I_{si}\left[1 - \sin\left(\varphi_s/2\right)\right]/\pi \\ P_{inv\_\text{sw}} = 2\sqrt{2}V_{\text{in}} I_{pi} f_s \cos\left(\frac{\varphi_p}{2}\right)\left(\frac{E_{sw\_\text{on}}+E_{sw\_\text{off}}}{V_R I_R} + \frac{Q_{RR}}{I_{RD}}\right) \\ P_{rec\_\text{sw}} = 2\sqrt{2}V_{\text{out}} I_{si} f_s \cos\left(\frac{\varphi_s}{2}\right)\left(\frac{E_{sw\_\text{on}}+E_{sw\_\text{off}}}{V_R I_R} + \frac{Q_{RR}}{I_{RD}}\right) \end{cases} \tag{9}$$

where R_{DS} is the equivalent on-state resistance, V_f is the threshold voltage, E_{sw_ON} and E_{sw_OFF} are the turn ON and turn OFF losses of MOSFET, V_R and I_R are the drain-source voltage and current of MOSFET, Q_{RR} and I_{RD} are the reverse recovery charge and the reference current of the diode.

The power loss of three-phase IGBT inverter is described as

$$P_{3\_inv} = P_{3inv\_con} + P_{3inv\_\text{sw}} \tag{10}$$

where $P_{3\,inv\_\text{con}}$ and $P_{3\,inv\_\text{sw}}$ denote the conducting and switching losses of three-phase inverter.

The switching and conducting losses of six IGBTs can be expressed as

$$\begin{cases} P_{3inv\_\text{sw}} = \frac{36V_{dc}i_L f_s}{\pi V_{ref} i_{ref}}\left(E_{3sw\_\text{on}} + E_{3sw\_\text{off}}\right) \\ P_{3inv\_con} = 6i_L V_{ce\_sat}\left(\frac{1}{8} + \frac{D}{3\pi}\cos(\theta_i)\right) \end{cases} \tag{11}$$

where f_s is the switching frequency, $E_{3\,sw\_\text{ON}}$ and $E_{3\,sw\_\text{OFF}}$ are the turn ON and turn OFF losses of IGBT, i_L is the peak value of the ac line current, V_{ref} is the blocking state voltage of the IGBT, i_{ref} is the on-state current, V_{ce_sat} is the IGBT saturation voltage drop at iL, D is the PWM duty cycle, and θ_i is phase angle between output voltage and current.

The power loss of PMSM can be expressed as

$$\begin{aligned} P_{mot} &= P_{Cu} + P_{Fe} \\ P_{Cu} &= \frac{3}{2}R_s i_s^2 \\ P_{Fe} &= K_h B_p \omega_e + K_e B_p^2 \omega_e^2 \end{aligned} \tag{12}$$

where P_{Cu} and P_{Fe} are the copper and core losses, K_h and K_e are the coefficients of hysteresis loss and excess loss, B_p is the peak value of the magnetic flux density, ω_e is the electrical angular speed, and R_a is the stator resistance.

As seen from (6)–(12), obviously, the power loss of wireless PMSM system is affected by multiple factors. Improving the

efficiency of wireless PMSM system from a control perspective is necessary and not a simple matter.

III. Design and Control of Wireless PMSM System With Variable DC-Link Voltage

A. Calculation of Variable DC-Link Voltage

From (10) and (11), it is obvious that the lower switching frequency or dc-link voltage can lead to the lower loss of three-phase inverter. To achieve the high-precision control of the PMSM, the switching frequency of three-phase inverter cannot be reduced to a low level. For the wireless PMSM system, the dc-link voltage is adjustable and can be added as a new control variable for improving the system efficiency and avoiding the occurrence of overmodulation and flux weakening control.

The mathematical model of interior PMSM in the *dq*-axis can be expressed as

$$\begin{cases} u_d = R_s i_d + L_d \frac{di_d}{dt} - \omega_e L_q i_q \\ u_q = R_s i_q + L_q \frac{di_q}{dt} + \omega_e (L_d i_d + \varphi_f) \end{cases} \tag{13}$$

where u_d and u_q denote the d-axis and q-axis voltages, i_d and i_q denote the d-axis and q-axis currents, L_d and L_q denote the d-axis and q-axis inductances, and φ_f denotes the permanent magnet flux linkage.

The electromagnetic torque T_e can be calculated as

$$T_e = \frac{3}{2} P_n \left[\varphi_f i_q + (L_d - L_q) i_d i_q \right] \tag{14}$$

where P_n is the number of pole pairs.

In the steady state, $did/dt = diq/dt = 0$, yielding that

$$\begin{cases} u_d \approx R_s i_d - \omega_e L_q i_q \\ u_q \approx R_s i_q + \omega_e (L_d i_d + \varphi_f). \end{cases} \tag{15}$$

Moreover, the maximum torque per ampere control, which generates the required torque using the minimum current magnitude, is generally adopted to minimize the copper loss of PMSM. Then,

$$i_d = \frac{-\varphi_f + \sqrt{\varphi_f^2 + 4(L_d - L_q)^2 i_q^2}}{2(L_d - L_q)}. \tag{16}$$

The minimum required dc-link voltage of PMSM system can be calculated by

$$\begin{aligned} V_{\text{dc\_min}} &= \sqrt{3} \times \sqrt{u_d^2 + u_q^2} \\ &= \sqrt{3} \times \sqrt{(R_s i_d - \omega_e L_q i_q)^2 + (R_s i_q + \omega_e L_d i_d + \omega_e \varphi_f)^2}. \end{aligned} \tag{17}$$

However, the formula calculation (FC) method using (16) for the minimum dc-link voltage is based on the ideal model of PMSM. The mismatched motor parameters induced by the temperature variation and inductance saturation may lead to a large calculation error of dc-link voltage. Calculation results of FC method with different PM flux linkages are shown in Fig. 6, where the superscript "−" denotes the parameters used in FC method. It is evident that the mismatched parameters could result in the calculation error of tens of volts. The excessive dc-link voltage could increase the loss of three-phase inverter, and the insufficient dc-link voltage may result in the motor failing to operate.

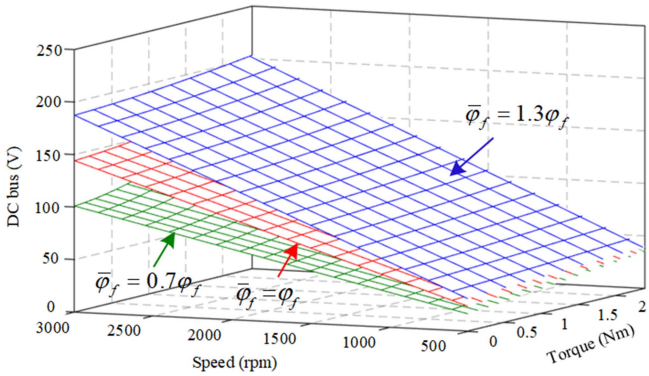

Fig. 6. Calculation results of FC method with different PM flux linkages.

Aiming at that, an ESO-VCM is proposed. The voltage error caused by nonideal factors can be estimated by ESO-VCM and written as

$$\begin{cases} \varepsilon_d = i_d - \hat{i}_d \\ \frac{d}{dt}\hat{i}_d = \frac{1}{\bar{L}_d}\left(u_d - \bar{R}_a i_d + \bar{L}_q \omega_e i_q + \Delta\hat{u}_d\right) + \beta_1 \varepsilon_d \\ \frac{d}{dt}\Delta\hat{u}_d = \bar{L}_d \beta_2 \varepsilon_d \end{cases} \tag{18}$$

$$\begin{cases} \varepsilon_q = i_q - \hat{i}_q \\ \frac{d}{dt}\hat{i}_q = \frac{1}{\bar{L}_q}\left(u_q - \bar{R}_a i_q - \bar{L}_d \omega_e i_d - \omega_e \bar{\varphi}_f + \Delta\hat{u}_q\right) + \beta_1 \varepsilon_q \\ \frac{d}{dt}\Delta\hat{u}_q = \bar{L}_q \beta_2 \varepsilon_d \end{cases} \tag{19}$$

where the superscript "^" denotes the estimation value, ε_d and ε_q are the estimated current errors, Δu_d and Δu_q are the *dq*-axis voltage errors, and β_1 and β_2 are the adjustable gains in the ESO-VCM. If $\beta_1 > 0$ and $\beta_2 > 0$, the Hurwitz stability criterion is satisfied and the estimation errors can converge exponentially to zero. Defining the coefficient ω_1 as the observer bandwidth, yielding

$$\beta_1 = 2\omega_1, \quad \beta_2 = \omega_1^2 \tag{20}$$

where ω_1 is the observer bandwidth.

The transfer function between estimated and actual voltage errors can be represented as (21), and the corresponding bode diagram with different ω is shown in Fig. 7. It is obvious that a large observer bandwidth corresponds to the fast convergence rate. However, it also makes the observer sensitive to noise. Considering the abovementioned factors, ω_1 is set to 500 rad/s in this article

$$G_{dq}(s) = \frac{\Delta\hat{u}_{d,q}}{\Delta u_{d,q}} = \frac{\omega_1^2}{s^2 + 2\omega_1 s + \omega_1^2}. \tag{21}$$

After obtaining the estimated voltage errors, the minimum required dc-link voltage can be calculated by

$$V_{\text{dc\_min}} = \sqrt{3} \times \sqrt{\begin{aligned} &\left(\bar{R}_s i_d - \omega_e \bar{L}_q i_q + \Delta\hat{u}_d\right)^2 + \left(\bar{R}_s i_q \right. \\ &\left. + \omega_e \bar{L}_d i_d + \omega_e \bar{\varphi}_f + \Delta\hat{u}_q\right)^2. \end{aligned}} \tag{22}$$

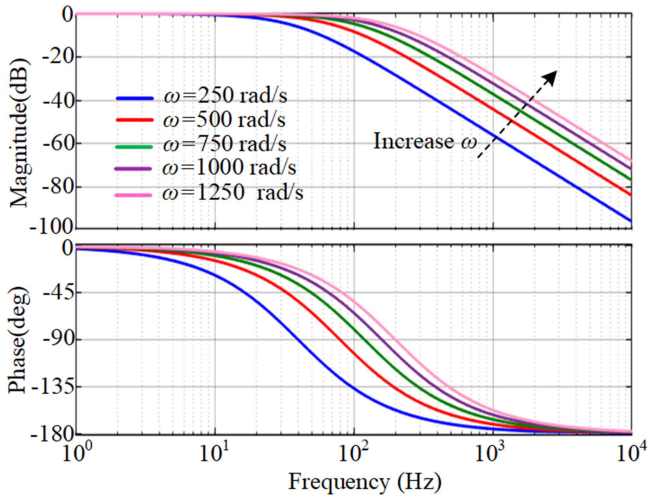

Fig. 7. Bode diagram of transfer function $G_{dq}(s)$ with different ω.

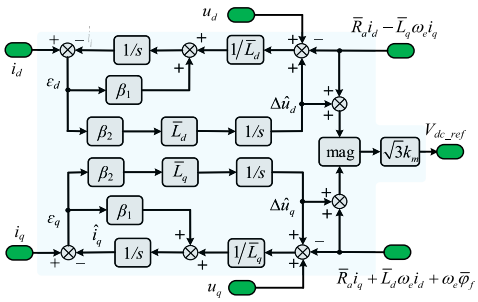

Fig. 8. Schematic diagram of ESO-VCM for variable dc-link voltage reference.

Considering the frequently varying working conditions of PMSM, a 5% margin is set for the dc-link voltage reference and expressed as

$$V_{\mathrm{dc}\_ref} = k_m V_{\mathrm{dc}\_\min} \tag{23}$$

where k_m ($k_m = 1.05$) is the margin factor. The schematic diagram of ESO-VCM for variable dc-link voltage reference is elaborated in Fig. 8.

B. Parameter Design of Wireless PMSM System With Variable DC-Link Voltage

From (5), ignoring the loss of active rectifier, the transmitted active power is approximately equal to the dc-link power, which is proportional to the dc-link voltage. Hence, the first step should be to determine the rough scope of variable dc-link voltage $V_{\mathrm{dc}\_\min}$ by adopting the FC or ESO-VCM methods.

Moreover, the dc-link power also depends on parameters of compensation networks. After determine the parameters of L_{pt} and L_{pi}, the parameters of C_{pt} and C_{ps} can be calculated by (4). Generally, the parameter and size of L_{pi} and L_{si} is first set according to users' requirements. Defining the ratio of the coil inductance and the compensation inductance as

$$\alpha = L_{pt}/L_{pi} = L_{st}/L_{si}. \tag{24}$$

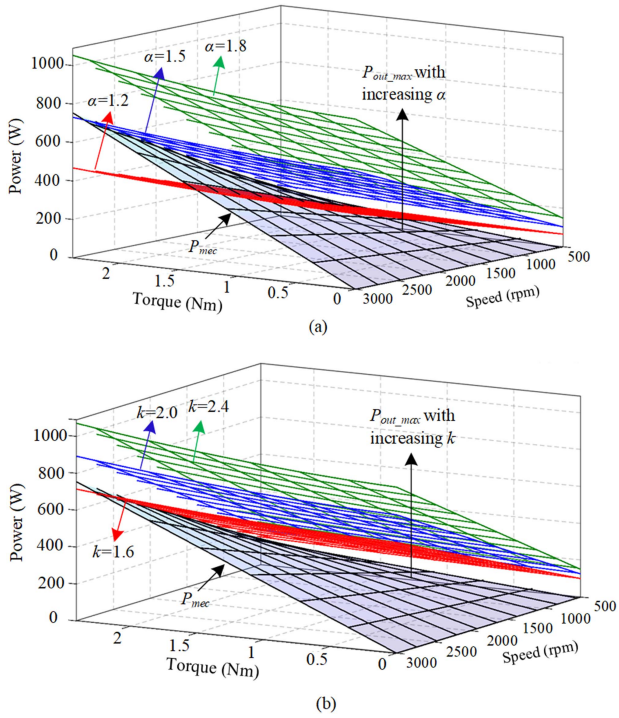

Fig. 9. Variation trends of $P_{\mathrm{out\_max}}$ and P_{mec} with different α and k.

Then, combining (5), (23), (24), $V_{\mathrm{dc}} = V_{\mathrm{dc}\_ref}$, $\varphi_p = \varphi_s = 180°$, and $\theta = 90°$, the maximum dc-link power can be calculated by

$$P_{\mathrm{out\_max}} = \frac{\alpha k V_{\mathrm{in}}}{\omega L_{pi}} k_m V_{\mathrm{dc\_min}} \propto \alpha k V_{\mathrm{dc\_min}}. \tag{25}$$

The variation trends of the maximum dc-link power $P_{\mathrm{out\_max}}$ and the mechanical power of PMSM P_{mec} ($=\omega_e T_e/P_n$) with different α and k are shown in Fig. 9. Under different speed and torque conditions, on the premise of ensuring the required dc-link voltage, the maximum dc-link power should be greater than the mechanical power of the PMSM. A suitable margin should be considered for the extra power loss, detuned parameters, and coil misalignment, which can be achieved by adjusting α for a certain range of k. As can be seen that the mismatched capacity typically occurs in the conditions of high-speed and heavy-load. Hence, the attention should be paid to the system capacity under the rated conditions or higher power conditions. Based on the above analysis, the flowchart of parameter design of wireless PMSM system with variable dc-link voltage can be summarized in Fig. 10.

C. Dynamic Improvement of Voltage Regulation Using FCS-MFPC Method

For the rapid regulation of dc-link voltage, a simple dynamic model of dc-link voltage based on the active rectifier is established as [26]

$$\frac{dV_{\mathrm{dc}}}{dt} = \frac{1}{C_f}(I_s - I_{\mathrm{dc}}) = \frac{2I_{si\mathrm{rms}}}{C_f \pi}\sqrt{1-\cos(\varphi_s)} - \frac{1}{C_f} I_{\mathrm{out}} \tag{26}$$

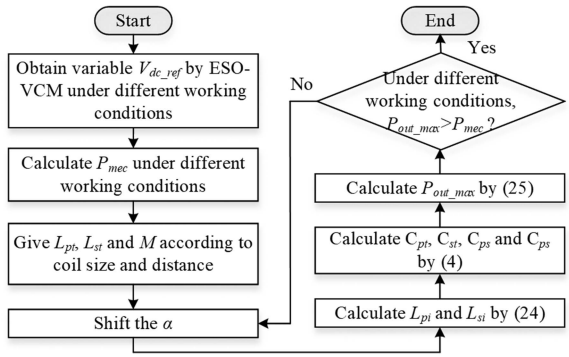

Fig. 10. Flowchart of parameter design of wireless PMSM system with variable DC-link voltage.

where $I_{si\mathrm{rms}}$ is the rms value of I_{si}.

To avoid the dependence of FCS-MPC controller on system parameters and extra current sensors, the ultralocal model is utilized to design the dc-link voltage controller. The ultralocal model of a single-input single-out system is described as

$$\frac{d}{dt}y = F + \alpha_m u \tag{27}$$

where u and y are control and output variables, α_m is the non-physical scaling factor designed by the users, and F represents the known and unknown part of the system.

Then, the ultralocal model of dc-link voltage can be expressed as

$$\frac{dV_{\mathrm{dc}}}{dt} = F + \alpha_m \sqrt{1-\cos(\varphi_s)} \tag{28}$$

where $\alpha_m = 2I_{si\mathrm{rms}}/\pi C_f$ is the gain of the input value, $F = -I_{\mathrm{out}}/C_f + \Delta f$ denotes the total disturbance, and Δf denotes the unmodeled disturbance.

According to the ultralocal model (28) of dc-link voltage, an ESO taking V_{dc} and F as state variables with the feedback of the dc-link voltage error can be designed as

$$\begin{cases} \varepsilon_{V\mathrm{dc}} = \hat{V}_{\mathrm{dc}} - V_{\mathrm{dc}} \\ \frac{d}{dt}\hat{V}_{\mathrm{dc}} = \hat{F} + \alpha_m \sqrt{1-\cos(\varphi_s)} + \beta_3 \varepsilon_{V\mathrm{dc}} \\ \frac{d}{dt}\hat{F} = -\beta_4 \varepsilon_{V\mathrm{dc}} \end{cases} \tag{29}$$

where β_3 and β_4 are the adjustable gains in the ESO for the ultralocal model. Similar to (21), defining ω_2 as the bandwidth of ESO for the ultralocal model, β_3 and β_4 satisfy that $\beta_3 = 2\omega_2$ and $\beta_4 = \omega_2^2$. To facilitate the design of FCS-MFPC, the ultralocal model can be discretized as

$$\begin{cases} \varepsilon_{V\mathrm{dc}}(k) = \hat{V}_{\mathrm{dc}}(k) - V_{\mathrm{dc}}(k) \\ \hat{V}_{\mathrm{dc}}(k+1) = \hat{V}_{\mathrm{dc}}(k) + T_p \\ \quad \left[\hat{F}(k) + \alpha_m(k)\sqrt{1-\cos(\varphi_s(k))} - \beta_3 \varepsilon_{V\mathrm{dc}}(k)\right] \\ \hat{F}(k+1) = \hat{F}(k) - T_p \beta_4 \varepsilon_{V\mathrm{dc}}(k) \end{cases} \tag{30}$$

where T_p is the control period of FCS-MFPC and $\alpha_m(k)$ can be further calculated as

$$\alpha_m(k) = \frac{2}{C_f \pi} I_{si\mathrm{rms}}(k) = \frac{4\sqrt{2}MV_{\mathrm{in}}}{\pi^2 \omega L_{pi} L_{si} C_f} \sin\left(\frac{\varphi_p(k)}{2}\right). \tag{31}$$

Actually, even if $\alpha_m(k)$ depends on the system parameters, the model errors induced by model mismatch can be categorized into the term of $\hat{F}(k+1)$ and compensated. The dc input voltage, primary-side phase shift angle and system parameters can be set to constant values, so that the wireless communication signals from primary-side controller can be avoided. Adopting the typical two-step prediction scheme [32], the final ultralocal model for the FCS-MFPC can be obtained as

$$V_{\mathrm{dc}}(k+2) = V_{\mathrm{dc}}(k) + T_p \left[\alpha_m(k)\left(\sqrt{1-\cos(\varphi_s(k))} + \sqrt{1-\cos(\varphi_s(k+1))}\right) + 2\hat{F}(k+1)\right]. \tag{32}$$

Based on the prediction model in (32), a cost function is designed to select the variation $\Delta\varphi$ ($\Delta\varphi = \varphi_s(k+1) - \varphi_s(k)$) of the phase shift angle φ_s to regulate the dc-link voltage V_{dc} to reference $V_{\mathrm{dc\_}ref}$ and expressed as

$$J = \left(V_{\mathrm{dc}}(k+2) - V_{\mathrm{dc\_}ref}\right)^2 + \alpha_1 \left(V_{\mathrm{dc}}(k+2) - V_{\mathrm{dc}}(k)\right)^2 \tag{33}$$

where the cost function contains two terms and α_1 ($\alpha_1 > 0$) is the weighting factor of the second term. The first term is relevant to the difference between predicted and reference voltages, which plays a dominant role while the actual voltage is far away from the reference. The second term takes effect as the actual voltage approaches the reference, which takes charge of voltage deviation reduction and disturbance suppression.

The control variable φ_s is continuous in nature, which should be discretized for the digital controller. Defining Δf as the minimum phase shift value that can be achieved in a digital controller, and it can be calculated as

$$\Delta f = 2\pi f_p / f_c \tag{34}$$

where f_c is the digital controller's clock frequency. Hence, the selection range of φ_s can be discretized into $n_{\max} = (\pi/\Delta f + 1)$ segments and expressed as

$$\varphi_s \in \{0, \Delta f, 2\Delta f, 3\Delta f, \ldots, \pi\}. \tag{35}$$

The finite control set of $\Delta\varphi$ can be designed for the rolling calculation as

$$\Delta\varphi \in \left\{-\frac{(n-1)\Delta f}{2}, \ldots, -\Delta f, 0, \Delta f, \ldots, \frac{(n-1)\Delta f}{2}\right\} \tag{36}$$

where n (n is odd and $n \geq 3$) denotes the number of elements of finite control set, and 0 is the center of finite control set.

It is obvious that Δf is related to the dynamic response and steady accuracy of FCS-MFPC. When the finite control set in (32) is adopted for the rolling calculation, the dynamic response is improved only by increasing the number of elements of finite control set. However, this would undoubtedly increase the computational burden of FCS-MFPC. Aiming at that, an

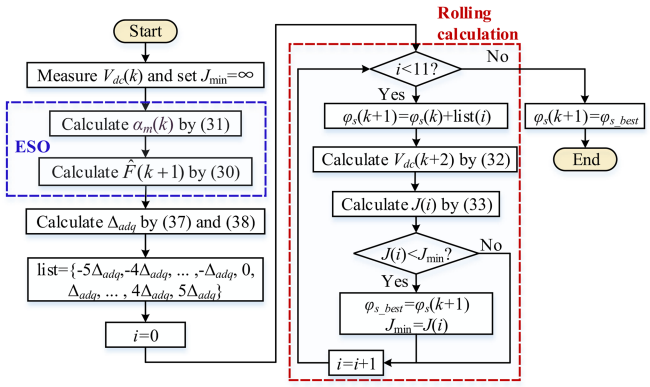

Fig. 11. Flowchart of the proposed FCS-MFPC.

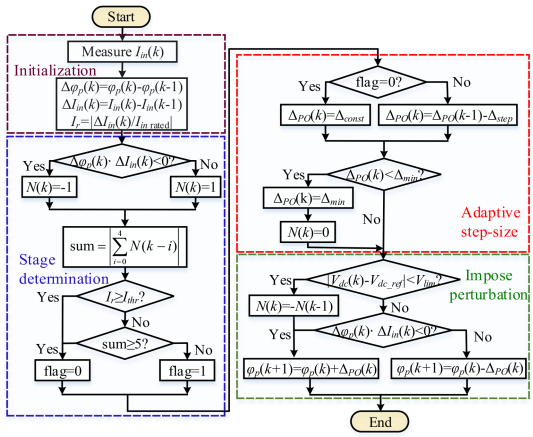

Fig. 12. Flowchart of the adaptive P&O method.

adaptive step-size Δ_{adp} is designed as

$$V_{err} = \begin{cases} V_m, & V_m \leq |V_{\mathrm{dc}\_ref} - V_{\mathrm{dc}}(k)| \\ |V_{\mathrm{dc}\_ref} - V_{\mathrm{dc}}(k)|, & |V_{\mathrm{dc}\_ref} - V_{\mathrm{dc}}(k)| < V_m \end{cases} \tag{37}$$

$$\Delta_{adp} = (1 + V_{err}) \cdot \Delta f \tag{38}$$

where V_m denotes the saturation voltage error. Δ_{adp} varies with the difference between V_{dc} and V_{dc_ref}. It increases as V_{dc} deviates from V_{dc_ref}, and when V_{dc} is regulated to V_{dc_ref}, Δ_{adp} is equal to Δf.

Combining with the adaptive step-size, the finite control set of $\Delta\varphi$ can be rewritten as

$$\Delta\varphi \in \left\{ -\frac{(n-1)\Delta_{adp}}{2}, \ldots, -\Delta_{adp}, 0, \Delta_{adp}, \ldots, \frac{(n-1)\Delta_{adp}}{2} \right\} \tag{39}$$

when the finite control set in (39) is adopted for the rolling calculation, the fast dynamic response can be guaranteed with a relatively small value of n, and n is set to 11 in this article. The flowchart of the proposed FCS-MFPC is concluded in Fig. 11.

D. Efficiency Optimization Using Adaptive P&O Method

In Section III-C, the variable dc-link voltage with fast dynamic response can be achieved by adopting ESO-VCM and FCS-MFPC methods. On the premise of ensuring the stable dc-link voltage, an advanced control strategy is crucial to adjust the phase shift angle φ_p for H-bridge inverter to reduce P_{res}, P_{inv}, and P_{rec}. From (7)–(9), it is difficult to obtain the optimized φ_p to track the maximum efficiency point with such complex nonlinear trigonometric function. However, the system output power and voltage can be regarded as constant in the steady state. Hence, the minimum system input power P_{in} can indirectly be achieved by adjusting φ_p to minimize the input current I_{in}.

Based on the abovementioned analysis, an adaptive P&O method is designed to obtain the optimal phase shift angle φ_p. The search process of the adaptive P&O method is shown in Fig. 12, which consists of four parts: initialization, status determination, generation of adaptive step-size, and perturbation imposing. First, the dc input current I_{in} is sampled, and the variations ($\Delta\varphi_p$ and ΔI_{in}) of φ_p and I_{in} and the current change rate I_r are calculated. $I_{in\mathrm{rated}}$ denotes the rated dc input current. Second, a variable N is designed to record the direction of disturbance. When the product of $\Delta I_{in}(k)$ and $\Delta\varphi_p(k)$ is less than 0, $N(k)$ is equal to 1; otherwise, $N(k)$ is equal to -1. The system state can be distinguished as tracking stage and oscillation stage by detecting the sum of N in t number of consecutive periods, which is expressed as

$$\mathrm{sum} = \left| \sum_{i=0}^{t-1} N(k-i) \right| \begin{cases} = t, & \text{tracking stage} \\ < t, & \text{oscillation stage} \end{cases} \tag{40}$$

where t is an integer not less than 3, and set to 5 in this article. While the maximum efficiency point is not found (sum $= 5$) or a significant load change occurs ($I_r > I_{thr}$, where I_{thr} is the threshold value designed by users), the system should be in the tracking stage (flag $= 0$) with a large perturbation step-size for the fast convergence. While the maximum efficiency point is found (sum<5), this means the system enters the oscillation stage(flag $= 1$), where the perturbation step-size should be small enough to avoid impact on the system.

After determining the system stage, an adaptive perturbation step-size Δ_{PO} is set as follows. For the tracking stage, a large constant step-size Δ_{const} is maintained to track the maximum efficiency point quickly. For the oscillation stage, Δ_{PO} is continuously decreased by Δ_{step} in each control period until it reaches a small value of Δ_{min}. Δ_{min} is maintained by setting $N(k)$ as 0 in response to a small load variation or external disturbance. Although the oscillation still exists in the system, Δ_{min} is so small that the oscillation can be ignored.

Eventually, enter the perturbation imposing process. The stable dc-link voltage should be first ensured. Hence, while $|V_{\mathrm{dc}}(k) - V_{\mathrm{dc}\_ref}| > V_{lim}$, $\varphi_p(k+1)$ should be increased by $\Delta_{PO}(k)$ to provide the required output power, and $N(k)$ is set to -$N(k$-1) so that the continuous perturbation with small step-size of Δ_{min} can be achieved within the required boundary of dc-link voltage. In other cases, judging whether the product of $\Delta I_{\mathrm{in}}(k)$ and $\Delta\varphi_p(k)$

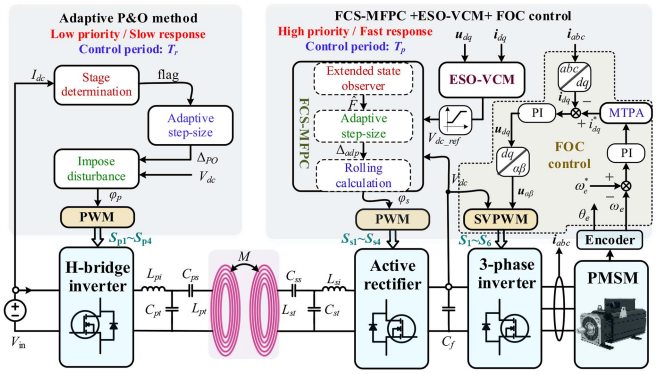

Fig. 13. Block diagram of overall control strategy of wireless PMSM system.

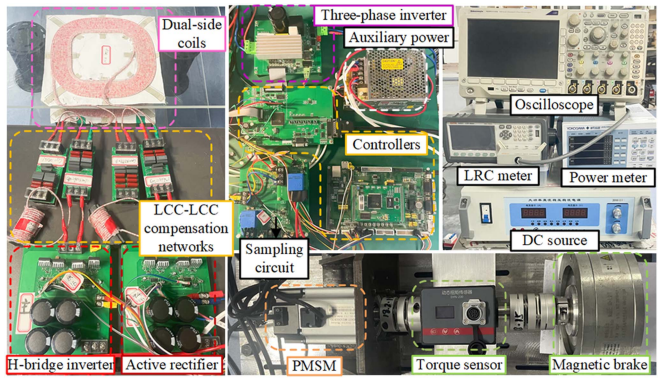

Fig. 14. Experimental setup of wireless PMSM system.

is less than 0. If so, $\varphi_p(k+1) = \varphi_p(k) + \Delta_{PO}(k)$. If not, $\varphi_p(k+1) = \varphi_p(k) - \Delta_{PO}(k)$.

E. Cooperative Control Principle of Wireless PMSM System

The cooperative control strategy of adaptive P&O method, FCS-MFPC, ESO-VCM, and FOC control is illustrated in Fig. 13. For the wireless PMSM system, the stable dc-link voltage and the reliable operation of PMSM have the highest priority. The dc-link voltage reference V_{dc_ref} is generated by the ESO-VCM, and a saturation function is added for the startup of PMSM and anti-overvoltage of dc-link voltage. The dc-link voltage is regulated by adopting the FCS-MFPC method in real time to track quickly the variable dc-link voltage provided by ESO-VCM, so that the required dc-link voltage of PMSM system can be guaranteed and robust. Moreover, the FOC control is utilized to regulate the rotor speed and phase currents of PMSM, and the drive signals of three-phase inverter is generated by combining the SVPWM scheme and the variable dc-link voltage. FCS-MFPC, ESO-VCM, and FOC control jointly serve the stable dc-link voltage and mechanical output power P_{mec} of PMSM, so they have the highest priority with the control period T_p. On the premise of ensuring the stable dc-link voltage, the adaptive P&O method is implemented with the control period T_r ($T_r << T_p$) to slowly adjust the phase shift angle φ_p to further improve the efficiency of wireless PMSM system. Moreover, it is noted that only a slow communication about the about dc-link voltage is required by primary-side controller to maintain the minimum system capacity.

V. Experimental Results

A. Experimental Setup

The experimental platform of double-LCC-compensated wireless PMSM system is established, as shown in Fig. 14 to test the effectiveness of the proposed strategy. The circuit parameters of wireless PMSM system are shown in Table I, and the control parameters of the proposed control strategy are shown in Table II. The coupled coils are made by the Litz wire composed of 300 varnished wires, and the air gap between the primary and secondary coils is set to 7 cm. The SiC MOSFETs (SCH2080KE) are adopted as switching devices for H-bridge inverter and active rectifier, and the IGBT module (FSBB30CH060) in the three-phase converter is adopted to generate the stator voltage for the PMSM. The DSP (TMS320F28335) is utilized as the digital controller to implement the control strategy. The phase synchronization of dual-side controllers is achieved by the method reported in [32], and the slow communication of the dc-link voltage is achieved by wireless communication RF module (NRF24L01+). The system efficiency and loss distribution are measured by the digital power meter (Yokogawa WT333E).

TABLE I
Circuit Parameters of Wireless PMSM System

Parameter	Value	Parameter	Value	Parameter	Value
V_{in}	200 V	C_{pt}	134.8 nF	C_f	940 μF
V_{dc}	80-250V	C_{st}	135.0 nF	R_s	0.93 Ω
L_{pt}	48.2 μH	R_{pt}	62.6 mΩ	L_d	4.03 mH
L_{st}	49.5 μH	R_{st}	60.1 mΩ	L_q	6.24 mH
L_{pi}	26.0 μH	R_{pi}	37.4 mΩ	φ_f	0.053 Wb
L_{si}	26.1 μH	R_{si}	32.2 mΩ	P_n	5
C_{ps}	158.0 nF	M	11.6 μH	n_N	3000 rpm
C_{ss}	149.5nf	f_s	85 kHz	I_N	4.2 A

where n_N denotes the rated speed and I_N denotes the rated current of PMSM.

TABLE II
Control Parameters of Proposed Control Strategy

Parameter	Value	Parameter	Value	Parameter	Value
T_p	100 μs	α_1	6	Δ_{min}	1.5 °
n	11	ω_2	1000 rad/s	V_{lim}	2 V
ω_1	500 rad/s	t	5	I_{thr}	0.5 A
Δf	0.204 °	Δ_{const}	15 °	T_r	100 ms
V_m	30 V	Δ_{step}	1.5 °		20 ms

B. Verification of Proposed ESO-VCM for Variable DC-Link Voltage

Experimental results about $V_{\mathrm{dc\_min}}$ acquired by FC method and ESO-VCM with PM flux variation are shown in Fig. 15, where the speed increases from 500 r/min and 2000 r/min and the torque is 1.2 N·m. It is obvious that the minimum required dc-link voltage $V_{\mathrm{dc\_min}}$ acquired by FC method is

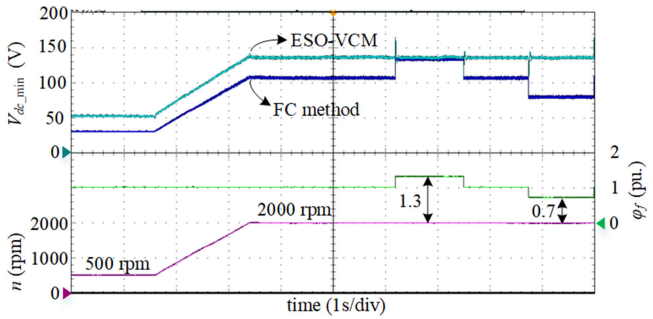

Fig. 15. Experimental results of FC method and ESO-VCM with PM flux variation.

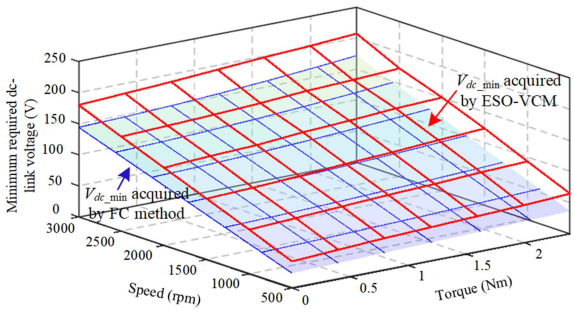

Fig. 16. Calculation result comparison of FC method and ESO-VCM under different operating conditions.

significantly less than that of ESO-VCM, due to the mismatch between parameters provided by the merchant and actual parameters. Moreover, the calculation result of FC method varies with the system parameters. The mismatched parameters can even lead to a calculation error of tens of volts. The excessive dc-link voltage can increase the converter loss, and the insufficient dc-link voltage can cause the failure of motor operation. After adopting the ESO-VCM, the parameter dependency can be overcome and the stable $V_{\mathrm{dc\_min}}$ can be obtained.

Calculation result comparison of FC method and ESO-VCM under different operating conditions is shown in Fig. 16. Calculation results of FC method utilizing parameters provided by merchant are about 20–40 V lower than that of ESO-VCM. Benefiting from the model-free characteristic of ESO-VCM, it can be approximated that estimated results of ESO-VCM correspond to the actual $V_{\mathrm{dc\_min}}$ acquired by PMSM. The range of dc-link voltage reference can be decided by the calculation results shown in Fig. 16. Considering a 5% margin, the range of dc-link voltage within the rated working conditions is set to 80–250 V.

Experimental results of wireless PMSM system with variable dc-link voltage using ESO-VCM are shown in Fig. 17, where the speed is increased from 500 r/min to 3000 r/min under the load of 1.2 N·m. The dc-link voltage reference increases with the rotor speed of PMSM, and the dc-link voltage can track the reference value from 80 to 202 V to ensure the stable operation of PMSM.

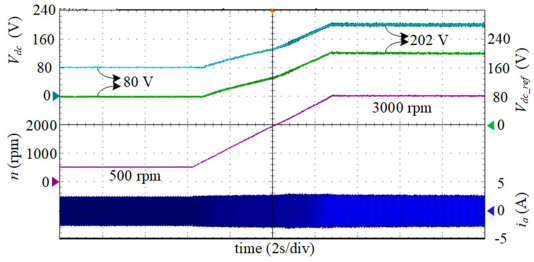

Fig. 17. Experimental results of wireless PMSM system with variable DC-link voltage using ESO-VCM under speed variation.

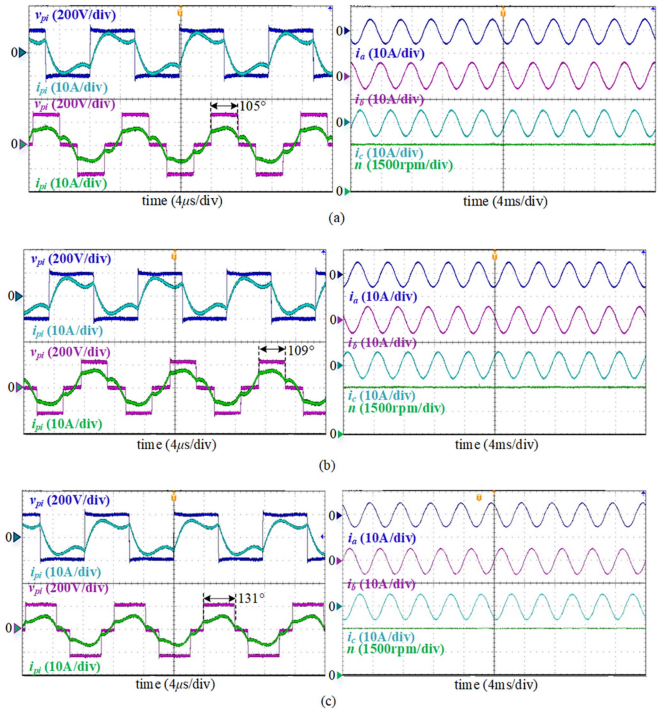

Fig. 18. Experimental waveforms of compensation network and PMSM system under the rated condition. (a) $V_{\mathrm{dc\_ref}} = 250$ V. (b) $V_{\mathrm{dc\_ref}} = 218$ V (acquired by ESO-VCM). (c) $V_{\mathrm{dc\_ref}} = 218$ V under the coil-misalignment ($k = 0.205$).

C. Capacity Verification of Wireless PMSM System

To test the capacity of the designed wireless PMSM system, experimental waveforms of compensation network and PMSM system under the rated condition are shown in Fig. 18, where the PMSM operates at 3000 r/min under the load of 2.4 N·m. The dc input voltage is 200 V and the phase shift angle φ_p is set to 180°. In Fig. 18(a), where the upper boundary of dc-link voltage reference is applied, the PMSM can operate steadily under the rated condition and the phase shift angle φ_s is about 105°. The output power of system can be further enhanced by increasing φ_s, which means the system has the sufficient capacity margin for the stable operation of PMSM. Moreover, as illustrated in Fig. 18(b), where the dc-link voltage reference is acquired by ESO-VCM, the peak value of v_{pi} is reduced to 218 V and the phase shift angle φ_s is increased to 109°. The phase currents and rotor speed are the same as that in Fig. 18(a). While ensuring the required dc-link voltage for PMSM, the system still has the

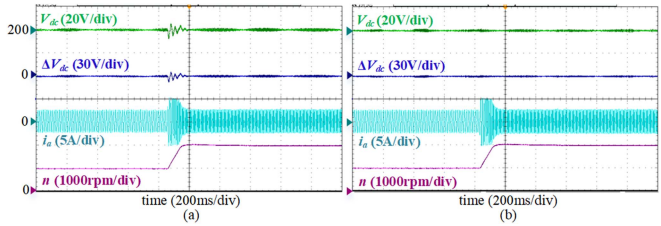

Fig. 19. Experimental results of wireless PMSM system with constant dc-link voltage under speed variation using the following terms. (a) PI control. (b) FCS-MFPC.

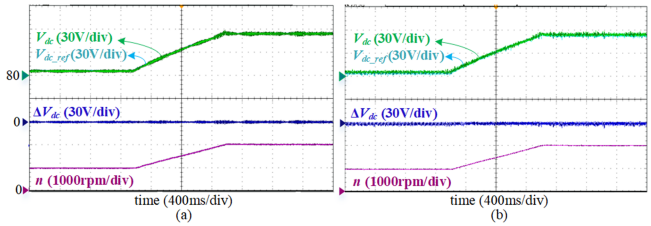

Fig. 20. Experimental results of wireless PMSM system with variable DC-link voltage under the slow speed variation using the following terms. (a) PI control. (b) FCS-MFPC.

sufficient capacity margin for meet the output power of PMSM. Furthermore, experimental results about system capacity under the horizontal coil-misalignment of 4 cm are shown in Fig. 18(c), where M is decreased from 11.6 μH to 10.0 μH and k is decreased from 0.237 to 0.205. The peak value of v_{pi} is still 218 V and the phase shift angle φ_s is increased to 131°. Under the coil-misalignment, the capacity margin of wireless PMSM system is still sufficient, which verifies the system capacity with designed parameters listed in Table I.

D. DC-Link Voltage Regulation Verification of FCS-MFPC

To evaluate the capacity of the proposed FCS-MFPC method, experimental results about dynamic response of wireless PMSM system with constant dc-link voltage using PI control and FCS-MFPC are first elaborated in Fig. 19, where the constant dc-link voltage of 200 V is applied and $\Delta V_{\rm dc}$ denotes the difference between actual and reference values of dc-link voltage. During the speed-up process, the phase current i_a is increased to generate the large electromagnetic torque, which would have an impact on the bus voltage. It is obvious that the PI control suffers from the large voltage fluctuation and long setting time during the speed-up process due to its inherent linear characteristics. However, for the proposed FCS-MFPC, the dc-link voltage $V_{\rm dc}$ presents no significant variation.

Furthermore, experimental results of wireless PMSM system with variable dc-link voltage under speed variation using PI control and FCS-MFPC are shown in Figs. 19 and 20, where the dc-link voltage reference is generated by ESO-VCM. As seen from Fig. 20(a) and (b) that during the slow speed-up process, both PI control and FCS-MFPC could ensure that the dc-link voltage tracks the reference value produced by ESO-VCM well. This indicates that the proposed FCS-MFPC has the steady-state

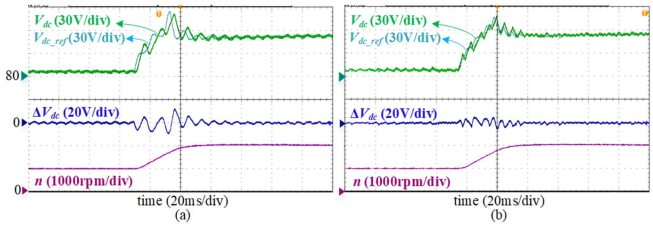

Fig. 21. Experimental results of wireless PMSM system with variable dc-link voltage under the rapid speed variation using the following terms. (a) PI control. (b) FCS-MFPC.

control performance similar to that of PI control. However, it is worth noting that the variable dc-link voltage reference is generated jointly by the FOC of PMSM system and the ESO-VCM, and the dc-link voltage is adjusted by the dc-link voltage controller to track the variable voltage reference and then applied to SVPWM scheme to serve the FOC of PMSM system. This means that the dc-link voltage control and the ESO-VCM for generating the variable dc-link voltage reference are mutually coupled. As illustrated in Fig. 21(a), during the rapid speed variation process under the load of 1.6 N·m, the tracking error about dc-link voltage of PI controller could further disturb the dc-link voltage reference produced by ESO-VCM. The interaction between tracking errors and reference errors results in the maximum up to 12 V, and the reaches 162 V. After adopting the proposed FCS-MFPC, benefiting from its great dynamic response, the tracking error of dc-link voltage is within ±5.5 V and the dynamic dc-link voltage is limited in 157 V. To sum up, the steady-state and dynamic performance of FCS-MFPC can be verified.

E. Efficiency Optimization Verification of Adaptive P&O Method

Subsequently, another test is taken to further validate the capacity of adaptive P&O method about efficiency optimization. Experimental results of wireless PMSM system at 2000 r/min with 1.2 N·m and at 3000 r/min with 1.2 N·m using adaptive P&O method are illustrated in Fig. 22. As seen from that after adopting the adaptive P&O method, the tracking stage and the oscillation state can be distinguished successfully. In the tracking stage, a large perturbation step-size of 15° is applied. While the system enters the oscillation stage, the large perturbation step-size is continuously decreased by 1.5° in each control period until it reaches the small value of 1.5°. Hence, the inevitable oscillation can be ignored due to the small perturbation step-size. As shown in Fig. 22(a), the system input current can be reduced from 1.80 to 1.64 A, which means the total system efficiency can be enhanced from 69.8% to 76.6%. As shown in Fig. 22(b), the system input current can be reduced from 2.56 to 2.46 A, which indicates the total system efficiency can be enhanced from 73.6% to 76.6%. Hence, it can be proved that the proposed adaptive P&O method is effective for the efficiency optimization of wireless PMSM system.

In some special working conditions, as the phase shift angle φ_p decreases continuously, the dc-link voltage may continue

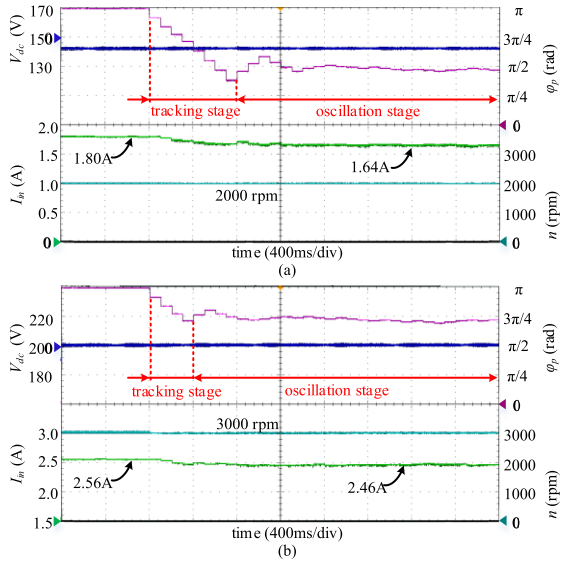

Fig. 22. Experimental results of wireless PMSM system using adaptive P&O method. (a) At 2000 r/min with 1.2 N·m. (b) At 3000 r/min with 1.2 N·m.

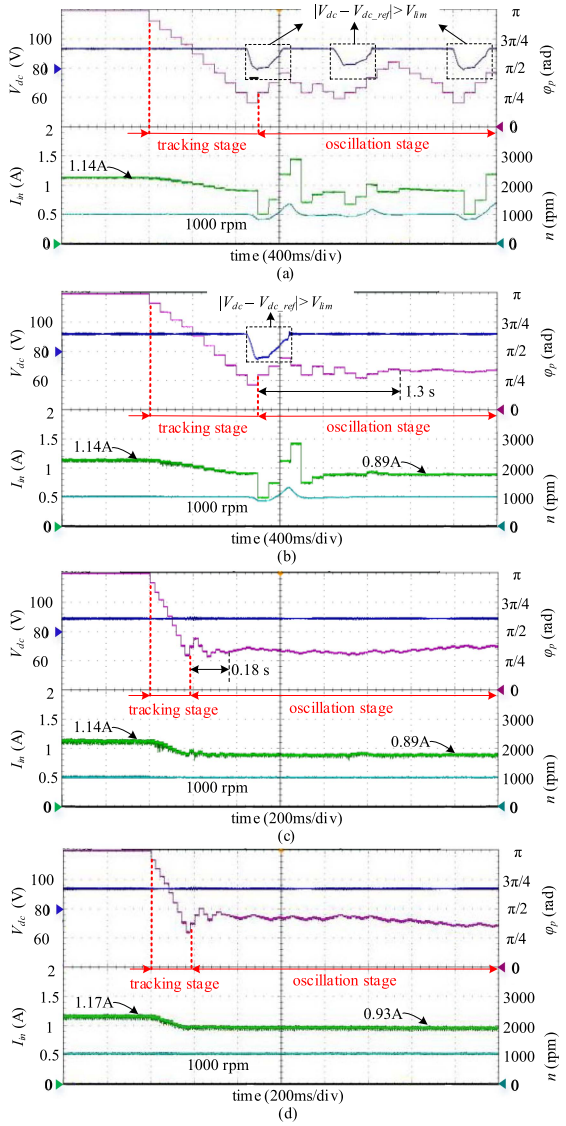

Fig. 23. Experimental results of wireless PMSM system using adaptive P&O method at 1000 r/min with 1.2 N·m. (a) Without $N(k) = -N(k\text{-}1)$ and with $T_r = 100$ ms (b) with $N(k) = -N(k\text{-}1)$ and $T_r = 100$ ms (c) with $N(k) = -N(k\text{-}1)$ and $T_r = 20$ ms. (d) With $N(k) = -N(k\text{-}1)$ and $T_r = 20$ ms under the coil-misalignment ($k = 0.205$).

to be less than the reference value for a while. In this paper, while $|V_{\rm dc}(k) - V_{\rm dc\_ref}| > V_{lim}$, $N(k)$ should be set to $-N(k\text{-}1)$ so that the continuous perturbation with small step-size of $\Delta_{\rm min}$ can be achieved within the required boundary of dc-link voltage to avoid the system power fluctuation. Experimental results of wireless PMSM system using adaptive P&O method at 1000 r/min with 1.2 N·m are shown in Fig. 23. As shown in Fig. 23(a), without $N(k) = -N(k\text{-}1)$, after the system reaches the minimum power boundary that maintains system operation, the system capacity oscillates at this power boundary, so that the dc input current, dc-link voltage, and rotor speed are continuously disturbed. This indicates that the system cannot converge at the minimum power boundary that maintains system operation. As shown in Fig. 23(b), with performing the operation of $N(k) = -N(k\text{-}1)$, when enabling the adaptive P&O method with the control period of 100 ms, after experiencing a significant voltage drop, the oscillation stage with the small step-size of 1.5° is achieved within the required boundary of dc-link voltage through a convergence of 1.3 s. The system input current is reduced from 1.14 to 0.89 A, which manifests the total system efficiency is enhanced from 55.1% to 70.5%. Benefiting from the dc-link voltage controller with fast dynamic response, the control frequency of adaptive P&O method can be further increased to enhance the convergence rate and reduce the drop of dc-link voltage. As shown in Fig. 23(c), where the control period T_r is shortened to 20 ms, there is no significant voltage drop observed, and the step-size in the oscillation stage can be decreased from 15° to 1.5° through a convergence process of 0.18 s. Furthermore, experimental results under the horizontal coil-misalignment of 4 cm are given in Fig. 18(d). Under the coil-misalignment, the system efficiency is slightly decreased. After enabling the adaptive P&O method, the system input current is reduced from 1.17 to 0.93 A, and the total system efficiency is enhanced from 53.6% to 67.5%. Therefore, the effectiveness of adaptive P&O method can be further verified. On the other hand, it is suggested that a relatively high control frequency of adaptive P&O method should be selected on the premise of ensuring the stability of dc-link voltage.

F. Efficiency Analysis of Proposed Wireless PMSM System

Power loss distributions of wireless PMSM system with different control strategies at 2000 r/min with 1.2 N·m and at 3000 r/min with 1.2 N·m are illustrated in Fig. 24, respectively. In the basic control method, the constant dc-link voltage is adopted and set to 250 V for the stable operation of the system. For the variable $V_{\rm dc}$ method, the dc-link voltage reference is variable and obtained by the ESO-VSM. The "variable $V_{\rm dc}$ + adaptive P&O" method represents the combination of variable

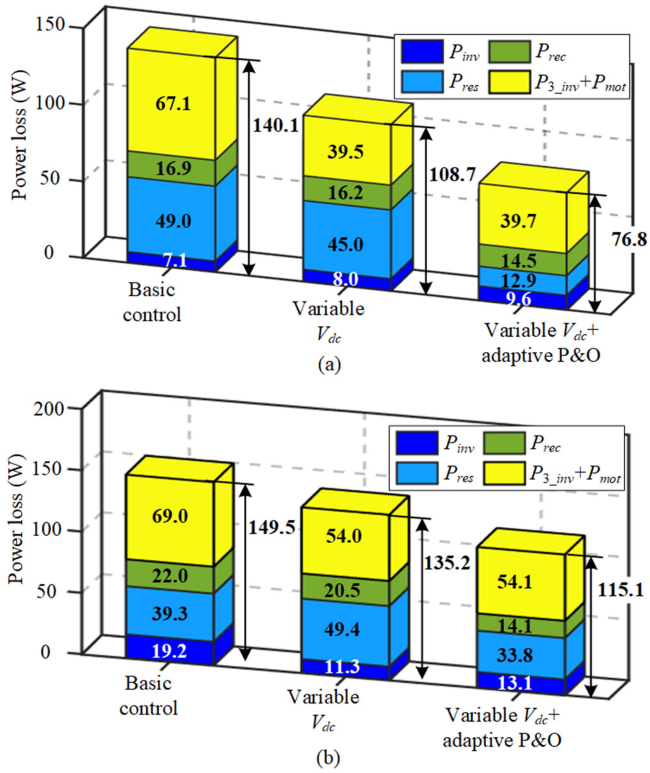

Fig. 24. Power loss distributions of wireless PMSM system with different control strategies. (a) At 2000 r/min with 1.2 N·m. (b) At 3000 r/min with 1.2 N·m.

$V_{\rm dc}$ method and adaptive P&O method. As shown in Fig. 24, the sum of P_{3_inv} and P_{mot} with variable $V_{\rm dc}$ method is significantly less than that with basic control method, and the sum of P_{inv}, P_{res}, and P_{rec} in these two methods is close. The power loss of PMSM can be reduced from 67.1 W to 39.5 W while the motor operates at 2000 r/min with 1.2 N·m, and from 69.0 W to 54.0 W while the motor operates at 3000 r/min with 1.2 N·m. Due to the use of SVPWM, the power loss of PMSM can be approximated as consistent for the constant and variable $V_{\rm dc}$ conditions. Therefore, it can be concluded that the variable $V_{\rm dc}$ leads to the smaller power loss of three-phase inverter, thereby improving the system efficiency to a certain extent. Further, by adopting the "variable $V_{\rm dc}$ + adaptive P&O" method, the sum of P_{inv}, P_{res}, and P_{rec} can be further optimized and reduced from about 70 W to about 37 W while the motor operates at 2000 r/min with 1.2 N·m, and from about 80 W to about 61 W while the motor operates at 3000 r/min with 1.2 N·m.

The comparison of the total system efficiency of wireless PMSM system with different control strategies under different operating conditions is illustrated in Fig. 25. The total system was calculated as the ratio of the mechanical output power of PMSM and the dc input system power. It is obvious that the introduction of variable dc-link bus voltage can improve the system efficiency to a certain extent, especially for the low-speed domain. After combining the variable dc-link bus voltage and adaptive P&O method, the total system efficiency can be further markedly improved, especially for the light-and-medium load.

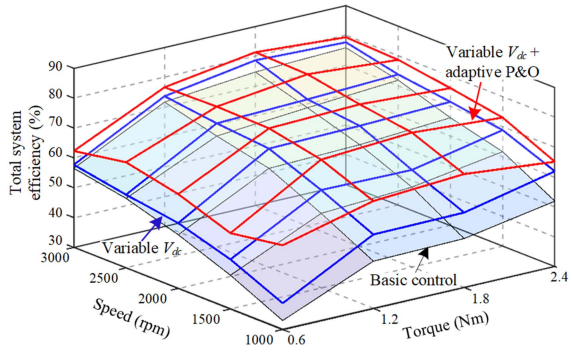

Fig. 25. Total system efficiency comparison of wireless PMSM system with different control strategies under different operating conditions.

The total system efficiency maintains over about 60% within the wide speed range, and the maximum system efficiency can reach about 80% under the working condition of high-speed and heavy load. To sum up, the effectiveness about efficiency optimization of proposed strategy can be verified.

V. Conclusion

In this article, a novel control scheme is proposed to achieve the efficiency optimization and dynamic improvement for wireless PMSM system with variable dc-link voltage. This article's conclusions and contributions are summarized as follows.

1) The operating mechanism of wireless PMSM system with the variable dc-link voltage is introduced in detail, and the corresponding design principles of parameters are given.
2) The ESO-VCM is deigned to obtain the minimum dc-link voltage reference, which can support the stable operation of the motor. The calculation result is robust to the parameter variations of PMSM.
3) The regulation of dc-link voltage with fast response is achieved by adopting the proposed FCS-MFPC, so that the dc-link voltage can quickly track the voltage reference generated by ESO-VCM. Moreover, FCS-MFPC does not rely on system parameters and extra sensors.
4) On the premise of ensuring the stable dc-link voltage, the adaptive P&O method is presented to slowly search for the optimal system efficiency point, so that the system efficiency can be further improved. Furthermore, the cooperative control principle of the above methods is given.

References

[1] J. Yin, D. Lin, C. K. Lee, T. Parisini, and S. Y. Hui, "Front-end monitoring of multiple loads in wireless power transfer systems without wireless communication systems," *IEEE Trans. Power Electron.*, vol. 31, no. 3, pp. 2510–2517, Mar. 2016.
[2] Q. Chen, S. C. Wong, C. K. Tse, and X. Ruan, "Analysis, design, and control of a transcutaneous power regulator for artificial hearts," *IEEE Trans. Biomed. Circuits Syst.*, vol. 3, no. 1, pp. 23–31, Feb. 2009.
[3] S. Chen, W. Ding, L. Huo, X. Wu, S. Shi, and R. Hu, "Dynamic improvement and efficiency optimization of wireless power transfer systems using improved FCS-MPC and P&O methods," *IEEE Trans. Power Electron.*, vol. 38, no. 11, pp. 14702–14718, Nov. 2023.
[4] H. Wang, W. Liu, and K. T. Chau, "A new breed of power electronics drives," in *Proc. Int. Conf. Power Electron. Syst.*, 2022, pp. 1–8.

[5] K. Deepak et al., "In-wheel motor drive systems for electric vehicles: State of the art, challenges," *Energies*, vol. 16, no. 7, 2023, Art. no. 3121.
[6] K. Li, W. Ding, J. N. Yuan, and C. L. Du, "A decoupled multichannel based wireless srm system with tunable compensation network and multifrequency pulse density control," *IEEE Trans. Ind. Electron.*, vol. 71, no. 2, pp. 1468–1480, Feb. 2024.
[7] J. H. Kim et al., "Development of 1-MW inductive power transfer system for a highspeed train," *IEEE Trans. Ind. Electron.*, vol. 62, no. 10, pp. 6242–6250, Oct. 2015.
[8] W. Han, K. T. Chau, Z. Hua, and H. Pang, "Compact wireless motor drive using orthogonal bipolar coils for coordinated operation of robotic arms," *IEEE Trans. Magn.*, vol. 58, no. 2, Feb. 2022, Art. no. 8200608.
[9] W. Liu, K. T. Chau, C. H. T. Lee, L. Cao, and W. Han, "Wireless power and drive transfer for piping network," *IEEE Trans. Ind. Electron.*, vol. 69, no. 3, pp. 2345–2356, Mar. 2022.
[10] C. Jiang, K. T. Chau, T. W. Ching, C. Liu, and W. Han, "Time-division multiplexing wireless power transfer for separately excited DC motor drives," *IEEE Trans. Magn.*, vol. 53, no. 11, Nov. 2017, Art. no. 8205405.
[11] C. Jiang, K. T. Chau, C. H. T. Lee, W. Han, W. Liu, and W. H. Lam, "A wireless servo motor drive with bidirectional motion capability," *IEEE Trans. Power Electron.*, vol. 34, no. 12, pp. 12001–12010, Dec. 2019.
[12] L. Fang et al., "Design of wireless individual-drive system for variable-reluctance stepping motor," *IEEE Trans. Circuits Syst. II, Exp. Briefs*, vol. 69, no. 4, pp. 2141–2145, Apr. 2022.
[13] C. Jiang, K. T. Chau, C. Liu, and W. Han, "Design and analysis of wireless switched reluctance motor drives," *IEEE Trans. Ind. Electron.*, vol. 66, no. 1, pp. 245–254, Jan. 2019.
[14] C. Jiang, K. T. Chau, W. Liu, C. Liu, W. Han, and W. H. Lam, "An LCC-compensated multiple-frequency wireless motor system," *IEEE Trans. Ind. Inform.*, vol. 15, no. 11, pp. 6023–6034, Nov. 2019.
[15] W. Ding, K. Li, J. N. Yuan, J. L. Li, and C. L. Du, "Wireless power transmission-based in-wheel switched reluctance motor drive system with an X-type converter," *IEEE Trans. Energy Convers.*, vol. 38, no. 1, pp. 450–462, Mar. 2023.
[16] H. Wang, K. T. Chau, C. H. T. Lee, L. Cao, and W. H. Lam, "Design, analysis, and implementation of wireless shaded-pole induction motors," *IEEE Trans. Ind. Electron.*, vol. 68, no. 8, pp. 6493–6503, Aug. 2021.
[17] H. Wang, K. T. Chau, C. H. T. Lee, and C. Jiang, " Wireless shaded-pole induction motor with half-bridge inverter and dual-frequency resonant network," *IEEE Trans. Power Electron.*, vol. 36, no. 12, pp. 13536–13545, Dec. 2021.
[18] P. Jin, L. Chang, Y. Liu, Y. Guo, G. Lei, and J. Zhu, "Design and implementation of novel rotor side brushless controller with bidirectional wireless power transmission for doubly-fed machine," *IEEE Trans. Ind. Electron.*, vol. 71, no. 1, pp. 183–193, Jan. 2024, doi: 10.1109/TIE.2023.3243312.
[19] M. Sato, G. Yamamoto, D. Gunji, T. Imura, and H. Fujimoto, "Development of wireless in-wheel motor using magnetic resonance coupling," *IEEE Trans. Power Electron.*, vol. 31, no. 7, pp. 5270–5278, Jul. 2016.
[20] C. Li, Z. Wang, and Y. Xu, "A wireless-power-transfer-based three-phase PMSM drive system with matrix converter," *IEEE Trans. Ind. Electron.*, vol. 70, no. 3, pp. 2307–2317, Mar. 2023.
[21] Y. Chen, C. Gan, H. Shi, K. Ni, and R. Qu, "Active power allocation strategy for a novel wireless open-winding motor system with improved anti-misalignment capability," *IEEE Trans. Ind. Electron.*, vol. 70, no. 12, pp. 12071–12081, Dec. 2023, doi: 10.1109/TIE.2023.3239869.
[22] Y. Huang, X. Gao, Z. Song, X. Liu, and C. Liu, "A novel wireless motor based on three-phase six-stator-winding PMSM," *IEEE Trans. Ind. Electron.*, to be published, doi: 10.1109/TIE.2023.3301548.
[23] C. Yu, J. Tamura, and R. D. Lorenz, "Optimum dc bus voltage analysis and calculation method for inverters/motors with variable DC bus voltage," *IEEE Trans. Ind. Appl.*, vol. 49, no. 6, pp. 2619–2627, Nov./Dec. 2013.
[24] S. Ko, Y.-K. Son, and S.-K. Sul, "Variable DC voltage shipboard power system with permanent magnet generator and diode front end," *IEEE Trans. Transp. Electrific.*, vol. 8, no. 3, pp. 3534–3545, Sep. 2022.
[25] Y. Chen, C. Gan, H. Shi, K. Ni, Z. Yang, and R. Qu, "Auxiliary circuit free maximum power efficiency tracking scheme for wireless motor system with source-load coupling," *IEEE Trans. Ind. Electron.*, vol. 70, no. 4, pp. 3414–3425, Apr. 2023.
[26] X. Zhang et al., "A control strategy for efficiency optimization and wide ZVS operation range in bidirectional inductive power transfer system," *IEEE Trans. Ind. Electron.*, vol. 66, no. 8, pp. 5958–5969, Aug. 2019.
[27] Y. Chen, C. Gan, H. Shi, K. Ni, and R. Qu, "Efficiency optimization and resilience improvement in wireless motor system with flexible DC-link voltage regulation," *IEEE Trans. Energy Convers.*, vol. 38, no. 3, pp. 1803–1814, Sep. 2023.
[28] F. Liu, K. Li, K. Chen, and Z. Zhao, "A phase synchronization technique based on perturbation and observation for bidirectional wireless power transfer system," *IEEE J. Emerg. Sel. Topics Power Electron.*, vol. 8, no. 2, pp. 1287–1297, Jun. 2020.
[29] K. Chen, J. Pan, Y. Yang, and K. W. E. Cheng, "Stability improvement and overshoot damping of SS-compensated EV wireless charging systems with user-end buck converters," *IEEE Trans. Veh. Technol.*, vol. 71, no. 8, pp. 8354–8366, Aug. 2022.
[30] S. Liu et al., "Dynamic improvement of inductive power transfer systems with maximum energy efficiency tracking using model predictive control: Analysis and experimental verification," *IEEE Trans. Power Electron.*, vol. 35, no. 12, pp. 12752–12764, Dec. 2020.
[31] R. P. Aguilera, P. Lezana, and D. E. Quevedo, "Finite-control-set model predictive control with improved steady-state performance," *IEEE Trans. Ind. Inform.*, vol. 9, no. 2, pp. 658–667, May 2013.
[32] Y. Tang, Y. Chen, U. K. Madawala, D. J. Thrimawithana, and H. Ma, "A new controller for bidirectional wireless power transfer systems," *IEEE Trans. Power Electron.*, vol. 33, no. 10, pp. 9076–9087, Oct. 2018.

Shuo Chen (Student Member, IEEE) was born in Shandong, China, in 1995. He received the B.S. degree from the Shandong University of Technology, Zibo, China, in 2017, and the M.S. degree from China University of Mining and Technology, Xuzhou, China, in 2020. He is currently working toward the Ph.D. degree with Xi'an Jiaotong University, Xi'an, China, all in electrical engineering.

His research interests include the wireless power transfer and drive control of permanent magnet synchronous motors.

Wen Ding (Member, IEEE) received the M.S. and Ph.D. degrees in electrical engineering from Xi'an Jiaotong University, Xi'an, in 2006 and 2009, respectively.

He is currently an Associate Professor with the School of Electrical Engineering, Xi'an Jiaotong University. His research interests include electrical machines and drives with emphasis on permanent magnet synchronous machines and reluctance machines, energy conversion systems, power electronics, electric vehicles, and wireless power transmission.

Lujie Huo (Student Member, IEEE) received the B.S. degree from China University of Mining and Technology, Xuzhou, China, in 2022. He is currently working toward the M.S. degree with the School of Electrical Engineering, Xi'an Jiaotong University, Xi'an, China, both in electrical engineering.

His research interests include the reduced dc-link capacitance permanent magnet synchronous motor drives and the sensorless control of permanent magnet synchronous motor.

Xiang Wu (Member, IEEE) was born in Jiangsu, China, in 1990. He received the B.S. and Ph.D. degrees in electrical engineering and automation from China University of Mining and Technology, Xuzhou, China, in 2013 and 2019, respectively.

He is currently a Lecturer of power electronics and electrical drives with the School of Electrical and Power Engineering, China University of Mining and Technology. His research interests include power electronics, modern control theory, battery management systems, and motor.